

# Interplay between magnetism and band topology in Kagome magnets $RMn_6Sn_6$

Y. Lee,<sup>1</sup> R. Skomski,<sup>2</sup> X. Wang,<sup>3</sup> P. P. Orth,<sup>1,4</sup> A. K. Pathak,<sup>5</sup> B. N. Harmon,<sup>1,4</sup> R. J. McQueeney,<sup>1,4</sup> and Liqin Ke<sup>1,\*</sup>

<sup>1</sup>*Ames Laboratory, U.S. Department of Energy, Ames, Iowa 50011*

<sup>2</sup>*Department of Physics and Astronomy, Nebraska Center for Materials and Nanoscience, University of Nebraska, Lincoln, Nebraska 68588*

<sup>3</sup>*Sophysics Technology, LLC*

<sup>4</sup>*Department of Physics and Astronomy, Iowa State University, Ames, IA, 50011*

<sup>5</sup>*Department of Physics, SUNY Buffalo State, Buffalo, New York 14222*

(Dated: January 28, 2022)

Kagome-lattice magnets  $RMn_6Sn_6$  recently emerged as a new platform to exploit the interplay between magnetism and topological electronic states. Using *ab initio* methods, we systematically investigate the electronic structures and intrinsic magnetic properties in  $RMn_6Sn_6$  with  $R = \text{Gd, Tb, Dy, Ho, and Er}$ . We reveal a non-monotonic dependence of the magnetocrystalline anisotropy energy on the spin quantization for all  $RMn_6Sn_6$ , except for  $R = \text{Gd}$ . Moreover, the Mn sublattice exhibits easy-plane anisotropy of similar amplitude in all  $RMn_6Sn_6$  compounds. Our results show that  $\text{TbMn}_6\text{Sn}_6$  has an easy-axis anisotropy, while  $\text{DyMn}_6\text{Sn}_6$  and  $\text{HoMn}_6\text{Sn}_6$  have easy-cone anisotropy, and  $\text{GdMn}_6\text{Sn}_6$  and  $\text{ErMn}_6\text{Sn}_6$  have easy-plane anisotropy. These numerical findings all agree well with the experiment and are fully consistent with the Mn coordination of the  $R$  atoms. The observed band structures of various  $RMn_6Sn_6$  compounds share great similarities near the Fermi level as they mainly consist of non- $4f$  bands. Multiple Dirac crossings occur at the Brillouin zone corners, opened by spin-orbit coupling (SOC). Most of these crossings are strongly  $k_z$ -dependent. The most prominent 2D-like Dirac crossing that can be effectively gapped by SOC lies  $\sim 0.7$  eV above the Fermi level, much higher than in previously reported band structures calculated in density functional theory [Ref. 1]. The inclusion of electron correlations within Mn- $3d$  electrons, however, can significantly lower this SOC-gapped crossing closer to the Fermi level, making it more relevant for the observation of topological phenomena. Finally, we predict an enhancement of the Mn magnetic moment on the  $RMn_6Sn_6$  surface, which may impact the topological band structures of surfaces or thin films, and is yet to be confirmed experimentally.

## I. INTRODUCTION

Two-dimensional (2D) Kagome-lattice of  $3d$  systems harbor Dirac crossings (DCs), flat bands, and electron correlations [1]. In the intrinsic ferromagnetic (FM) Kagome lattice, the spin-orbit coupling (SOC) and the breaking of time-reversal symmetry introduce a gap at Dirac points, resulting in Chern gapped insulators [2–4]. When these topological electronic states are near the Fermi level, large Berry curvatures are manifested, resulting in novel quantum properties such as the quantum anomalous Hall effect (QAHE).

Magnetism enriches the possibilities of topological state realizations and offers a mechanism of controlling them. For example, in the FM Kagome Chern insulators, the size of the Chern gap is determined by the orbital characters of corresponding bands as well as the size of the spin projection along the direction normal to the Kagome layer [2]. Unfortunately, it is not common that the magnetic order in the Kagome lattice has a robust out-of-plane spin alignment, which is necessary for generating the Chern gap. Recently, Yin and coworkers discovered the Chern topological magnetism in  $\text{TbMn}_6\text{Sn}_6$  [1]. The rare-earth Tb atoms, possessing a strong easy-axis magnetocrystalline anisotropy (MA),

antiferromagnetically couple with the Mn atoms and align the Mn spins along the out-of-plane direction below the spin-reorientation temperatures  $T_{\text{SR}}$ . This discovery of quantum-limit Chern topological magnetism in  $\text{TbMn}_6\text{Sn}_6$  has rekindled the interest in the  $RMn_6Sn_6$  family of compounds, where different  $R$  atoms and correspondingly a variety of magnetic structures provide a rich platform to explore quantum phenomena [5–14].

The magnetic structures of  $RMn_6Sn_6$  are determined by the single-ion MA of  $R$ - $4f$  orbitals and MA of the Mn sublattice, the exchange couplings between the  $R$ -Mn and within the Mn sublattices, and their temperature dependence. As a result, the topological electronic states will evolve with  $R$  and temperature. Understanding the magnetism in  $RMn_6Sn_6$  is necessary to explore further their potential topological electronic structure in real applications at finite temperature. In general, it is believed that the Mn sublattice in  $RMn_6Sn_6$  has an easy-plane MA. At low temperatures,  $R$  atoms with an open  $4f$  shell can have a stronger MA and coerce the Mn spin out of the basal plane. At higher temperatures, the easy-plane MA of Mn survives better and overcomes the MA of  $R$  atoms, resulting in a spin-reorientation. The R-Mn coupling also affects the interlayer magnetic ordering of Mn sublattices. Experiments have shown that  $RMn_6Sn_6$  where  $R = \text{Tb, Dy, and Ho}$  are collinear ferrimagnets at lower temperatures and reorient the spin into the basal plane before the compounds become completely spin-disordered [15–21].  $\text{ErMn}_6\text{Sn}_6$  has an antiferromagnetic (AFM) Mn order at

\* liqinke@ameslab.gov

high temperature before the Er magnetic sublattice ordering results in overall ferrimagnetic (FI) order at low temperature [16, 20, 22–25].

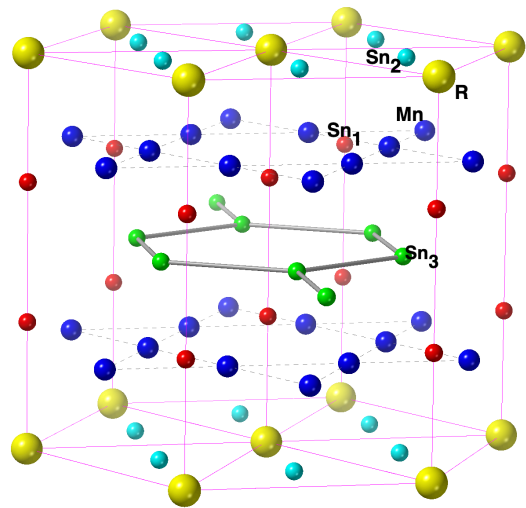
It is important to have DCs and gap opening near  $E_F$  for practical applications that utilize the effective topological edge states. Band structures near the Fermi level have been calculated in  $\text{TbMn}_6\text{Sn}_6$  [1] and other  $\text{RMn}_6\text{Sn}_6$  compounds, showing multiple DCs at the Brillouin zone (BZ) corners and gap opening by SOC. For  $\text{TbMn}_6\text{Sn}_6$ , a SOC-induced gap opens at the Dirac point, mainly consisting of in-plane Mn orbitals, at 0.2 eV above the Fermi level has been found in density functional theory (DFT) calculations [1]. Experimentally, Ma and coworkers [5] systematically investigated the topological transport in the  $\text{RMn}_6\text{Sn}_6$  family and found that the effective Chern gap and the Dirac cone energy decrease from  $R = \text{Gd}$  to Er. However, how electronic structures evolve with  $R$  elements and temperatures through spin reorientation is not well understood. Moreover, besides the  $4f$  orbitals, the electron correlations of Mn- $3d$  states may also need to be treated beyond plain DFT. As we will show later, additional electron correlations on the Mn sublattice can shift the Chern gap closer to  $E_F$  and become more relevant to experiments. Therefore, a comprehensive investigation of electronic structures and magnetic properties is desired.

In this work, we investigate the electronic structures and intrinsic magnetic properties of  $\text{RMn}_6\text{Sn}_6$  with  $R = \text{Gd}, \text{Tb}, \text{Dy}, \text{Ho}, \text{and Er}$ . We demonstrate that the magnetization, exchange coupling, and magnetocrystalline anisotropy can be well described using *ab initio* methods. Furthermore, we discuss the effects of spin-reorientation, the surface, and additional electron correlation of Mn- $d$  states on the topological band structures.

## II. THEORY AND METHODS

### A. Crystal structure

$\text{RMn}_6\text{Sn}_6$  with heavy  $R$  elements crystallizes in the Hexagonal  $\text{HfFe}_6\text{Ge}_6$ -type (or equivalently  $\text{MgFe}_6\text{Ge}_6$ -type;  $P6/mmm$ , space group no. 191) structure. The primitive cell contains one formula unit (f.u.). Figure 1 shows the crystal structure, where the primitive cell is tripled to illustrate the Mn kagome lattice better.  $R$  atoms occupy the  $1a(6/mmm)$  site, forming a triangular lattice in the basal plane.  $\text{Sn}_2$  atoms occupy the  $2d(\bar{6}m2)$  site located at the center of the  $R$  triangles, forming a honeycomb lattice; vice versa,  $R$  atoms are located in the centers of  $\text{Sn}_2$  hexagons. Mn atoms occupy the  $6i(2mm)$  site, forming two layers of the Kagome lattice in the unit cell.  $\text{Sn}_1$  atoms occupy the  $2e(6mm)$  site, forming two layers of triangular lattice, adjacent to the Mn layers.  $\text{Sn}_1$  atoms form  $-\text{Sn}_1-\text{Sn}_1-R-$  chains along the  $c$  axis with  $R$  atoms and are pushed slightly off the Mn Kagome plane by  $R$  atoms.  $\text{Sn}_3$  atoms occupy the  $2c(6m2)$  site, similar to  $\text{Sn}_2$ , forming a honeycomb lattice



$R$	Easy direction	$R$ -spin	Mn-spin
Tb	out of plane	$\uparrow\uparrow$	$\downarrow\downarrow$
Dy, Ho	tilted	$\nearrow\searrow$	$\swarrow\nwarrow$
Sc, Y, Lu	in-plane	zero	$\rightleftharpoons\rightleftharpoons$
Gd, Er, Tm, Yb	in-plane	$\rightarrow\rightarrow$	$\rightleftharpoons\rightleftharpoons$

FIG. 1. Crystal structure and magnetic ordering of  $\text{RMn}_6\text{Sn}_6$  [15, 16, 26–29] at low temperature. The primitive unit cell is tripled to better illustrate the Mn Kagome lattice.

by itself and sandwiched between two  $\text{Sn}_1$  layers. These layers are stacked in the order of  $[R-\text{Sn}_2]-\text{Mn}-\text{Sn}_1-\text{Sn}_3-\text{Sn}_1-\text{Mn}-[R-\text{Sn}_2]$  along the  $c$  axis.

Lattice parameters change with  $R$ . Experiments found that  $\text{TbMn}_6\text{Sn}_6$  has the largest volume, while  $\text{GdMn}_6\text{Sn}_6$  has the smallest volume. For all  $\text{RMn}_6\text{Sn}_6$  except  $\text{TbMn}_6\text{Sn}_6$ , the distance between neighboring Mn layers are slightly larger across the  $\text{Sn}_1$  and  $\text{Sn}_3$  layers than the one across the  $[R-\text{Sn}_2]$  layer. These two inter-Mn-plane distances are accidentally the same in  $\text{TbMn}_6\text{Sn}_6$ . The crystal structure can also be described as a filled derivative of the  $\text{CoSn } B35$ -type structure and closely related to the  $\text{CaCu}_5$ -type [30] and  $\text{ThMn}_{12}$ -type [31] structures [15].  $\text{RMn}_6\text{Sn}_6$  with light  $R$  elements have a different crystal structure.

### B. Methods for calculating electronic structures

DFT calculations are performed using a full-potential linear augmented plane wave (FP-LAPW) method, as implemented in WIEN2K [32]. The generalized gradient approximation of Perdew, Burke, and Ernzerhof [33] is used for the correlation and exchange potentials. To generate the self-consistent potential and charge, we employed  $R_{\text{MT}} \cdot K_{\text{max}} = 8.0$  with muffin-tin (MT) radii

$R_{\text{MT}} = 2.7, 2.4$ , and  $2.5$  a.u., for  $R$ , Mn, and Sn, respectively. The calculations are performed with 264  $k$ -points in the irreducible Brillouin zone (IBZ). They are iterated until charge differences between consecutive iterations are smaller than  $10^{-3} e$  and the total energy differences lower than  $0.01$  mRy. Low-temperature experimental lattice parameters [15] are adopted in all bulk calculations, and SOC is included using a second variational method.

The strongly correlated  $R$ - $4f$  electrons are treated in both the DFT+ $U$  method using the fully-localized-limit (FLL) double-counting scheme and the so-called open-core approach. For DFT+ $U$  calculations, the initial orbital occupancy of  $4f$  states are controlled to ensure that the self-consistent electron configurations satisfy Hund's rules and consistent with experiments. It is worth noting that DFT+ $U$  may not find the correct experimental  $R$ - $4f$  configurations as the ground states. To properly describe magnetic properties, especially  $R$ - $4f$  magnetocrystalline anisotropy, it is crucial to converge the DFT+ $U$  calculations to the solutions that are consistent with experiments. In the open-core approach, occupied  $4f$  electrons are included as core states, which is a reasonable approximation when describing the band structures near the Fermi level with negligible  $4f$  contributions. Moreover, we use the open-core approach to investigate the contributions of non- $4f$  electron on MA. Besides the  $R$ - $4f$  orbitals, we also explore the effects of Mn- $3d$  electron correlation on band structure near  $E_F$  by applying Hubbard  $U$  on Mn- $3d$  orbitals in DFT+ $U$  while treating  $R$ - $4f$  in the open-core approach. Considering the more itinerant nature of Mn- $d$  states in metallic  $RMn_6Sn_6$ , we mainly use the around-mean-field (AMF) double-counting scheme, which is also found to describe better the Mn magnetic moment than the FLL scheme in  $RMn_6Sn_6$ .

The band structures near  $E_F$  are further analyzed using an in-house *ab initio* tight-binding (TB) framework [34]. Realistic TB Hamiltonians are constructed via the maximally localized Wannier functions (MLWFs) method [35] as implemented in WANNIER90 [36] through a post-processing procedure [35, 37, 38] using the output of the self-consistent DFT calculations. We construct the TB Hamiltonian using 118 MLWFs, which correspond to  $d$ -type orbitals for  $R$  and Mn, and  $s$ - and  $p$ -type orbitals for Sn in the unit cell. Note that the 59 orbitals are doubled to account for SOC, which mixes the two spin channels. A real-space Hamiltonian  $H(\mathbf{R})$  with dimensions  $118 \times 118$  is constructed to accurately represent the band structures in the energy window of interest.

### C. Magnetocrystalline anisotropy in Rare-earth compounds

In general, the Mn spins in  $RMn_6Sn_6$  prefer the in-plane direction while the easy-axis of the  $R$  atoms varies with the type of  $R$  atom and may be incompatible with Mn. For the  $R$  sublattice, due to the strong

SOC, electronic configurations of  $4f$  shell obey the third Hund's rules [39]. The magnetic moment of  $4f$  electrons is strongly coupled with the anisotropic-shaped charge cloud, which is determined by superposing the occupied spherical harmonics of  $|l = 3, m\rangle$  with various  $m$  channels. The charge cloud orients accordingly with respect to the crystal field of surrounding lattices to minimize the Coulomb energy, giving the strong  $4f$ -electron MA.

To identify the easy direction and MA energy (MAE) of  $RMn_6Sn_6$ , we calculate the total energies of their collinear (ferrimagnetic) states in DFT+ $U$  as a function of magnetic quantization direction. The calculations are controlled to converge to the solutions consistent with experiments, in which the  $R$ - $4f$  electron configurations satisfy Hund's rules. Furthermore, we also use various approaches to resolve the MAE contribution into different sublattices. For example, to explore the non- $4f$  contribution to MAE dominated at high temperatures, we include  $R$ - $4f$  in the open core and constrain their moments to be zero to mimic a disordered  $4f$  moment. On the other hand, we also investigate the  $R$ -only contribution by turning off the SOC on Mn and Sn sites in MAE calculations.

### D. Spin-orientation-dependence of electronic structure

The magnetic structures, more specifically, the spin orientations of  $R$  and Mn atoms, are known to evolve with  $R$  and temperature. The moment directions and sizes directly impact the topology of the electronic band structure, and we calculate how band structures near  $E_F$ , especially the position of DCs and SOC-induced gap openings, depend on spin orientations.

As we show later, the Dirac bands are mainly characterized by non- $4f$ , mostly the Mn- $3d$  orbitals. The sizes of SOC-induced gaps and their dependence on the spin-quantization-axis direction can be understood by including the spin-orbit coupling (SOC) term in the single-particle Hamiltonian within a perturbation theory [40]. For an arbitrary spin-quantization direction  $\hat{\mathbf{n}} = (\theta, \varphi)$ , the SOC Hamiltonian can be written as

$$H_{\text{so}}(\hat{\mathbf{n}}) = \frac{\xi}{2} U(\theta, \varphi) (\mathbf{L} \cdot \mathbf{S}) U^\dagger(\theta, \varphi). \quad (1)$$

Here,  $\xi$  is the SOC constant depending on orbital  $l$  and site  $i$ , and  $U(\theta, \varphi)$  is the unitary transformation Wigner matrix (See details in Appendix A in Ref. [34]). Thus, we obtain

$$H_{\text{so}}(\theta, \varphi) = \frac{\xi}{2} \begin{pmatrix} A & B \\ B^\dagger & -A \end{pmatrix}, \quad (2)$$

where the spin-parallel component  $A$  and the spin-flip

TABLE I. The spin magnetic moment  $m_R^s$  and orbital magnetic moment  $m_R^l$  of  $R$  atom (in  $\mu_B/R$ ), the total magnetic moments of Mn atom  $m_{\text{Mn}}$  (in  $\mu_B/\text{Mn}$ ), and magnetization  $M$  (in  $\mu_B/\text{cell}$ ) in  $RMn_6\text{Sn}_6$  and compared to experiments.  $R-4f$  orbitals are treated within DFT+ $U$ . The calculated  $m_{\text{Mn}}$ , consisting of  $\sim 1\%$  orbital magnetic moment, is antiparallel with  $R$  moment. Sn atoms have a moment of  $\sim 0.11 \mu_B/\text{Sn}$ , and the interstitial has a moment of  $\sim 0.5 \mu_B/\text{f.u.}$ ; both align AFM with respect to the Mn moments. Electron occupancy in the minority  $R-4f$  channel  $n_{4f}^\downarrow$ , spin magnetic moment  $m_{4f}^s$ , orbital magnetic moment  $m_{4f}^l$ , and total magnetic moment  $m_{4f}$  of  $R-4f$  electrons, according to Hund's rules, are also shown. On-site spin and orbital magnetic moments are in units of  $\mu_B/\text{atom}$ . Experimental spin-reorientation temperature  $T_{\text{SR}}$  (in K) and Curie temperature  $T_C$  (in K) values are also listed.

$R$	$Z$	Hund's Rules				Calculations					Experiments					
		$n_{4f}^\downarrow$	$m_{4f}^s$	$m_{4f}^l$	$m_{4f}$	$m_R^s$	$m_R^l$	$m_R$	$m_{\text{Mn}}$	$M$	$m_R$	$m_{\text{Mn}}$	$M$	$T_{\text{SR}}$	$T_C$	References
Gd	64	0	7	0	7	7.33	-0.02	7.31	2.38	5.83	6.5	2.5	8.5		435–445	[16, 19, and 22]
Tb	65	1	6	3	9	6.26	2.96	9.23	2.42	4.10	9.2	2.39	5.77	310–330	423–450	[16, 19, 22, and 41]
Dy	66	2	5	5	10	5.21	4.96	10.18	2.40	3.05	9.97	2.11	2.69	270–320	393–410	[16, 19, and 22]
Ho	67	3	4	6	10	4.17	5.97	10.14	2.39	3.07	8.43	2.39	3.26–5.91	175–200	376–400	[16 and 19]
Er	68	4	3	6	9	3.19	5.93	9.12	2.38	4.03	8.40	2.21	4.86	75	340–352	[16, 22, and 23]

component  $B$  are written as

$$A(\theta, \varphi) = \cos(\theta)L_z + \frac{1}{2}\sin(\theta)(e^{i\varphi}L_- + e^{-i\varphi}L_+) \quad (3)$$

$$B(\theta, \varphi) = -\sin(\theta)L_z + \frac{1}{2}\left((\cos(\theta) + 1)e^{i\varphi}L_- + (\cos(\theta) - 1)e^{-i\varphi}L_+\right). \quad (4)$$

### III. RESULTS ON MAGNETIC PROPERTIES

#### A. Spin and orbital magnetic moments

Table I summarizes the magnetic moments and their components in  $RMn_6\text{Sn}_6$  calculated in DFT+ $U$  and compared with experimental values and the corresponding values expected for  $4f$  shells from Hund's rules. Previously reported experimental spin-reorientation temperatures and Curie temperatures are also listed for comparison. The experimental collinear magnetic structure and corresponding easy directions are adopted in the calculations.

The  $R-5d$  atoms are primarily spin-polarized by the neighboring 12 magnetic Mn atoms through the  $3d-5d$  hybridization and further enhanced by the on-site  $4f$  moment. The Mn spin aligns antiferromagnetically with the  $R-5d$  spin, which is parallel with the  $R-4f$  spin, resulting in  $R$ -Mn ferrimagnetic ordering in  $RMn_6\text{Sn}_6$ . Without considering the lattice parameters variation with  $R$ , the induced  $5d$  spin moment can be written approximately as

$$m_{5d}^{(R)} = 12\alpha m_{3d}^{(\text{Mn})} + \beta m_{4f}^{(R)}, \quad (5)$$

with  $\alpha \approx 0.007$  and  $\beta \approx 0.02$ . The  $5d$  spin moment decreases with the  $4f$  spin moment and by  $\sim 40\%$  when  $R$  goes from Gd to Er.

The calculated magnetic moments, as summarized in Table I, show good overall agreement with previously reported experimental values. Mn moments are calculated to have values of 2.38–2.42  $\mu_B/\text{Mn}$ , consistent with the reported experimental values of 2.11–2.5  $\mu_B/\text{Mn}$  in various  $RMn_6\text{Sn}_6$  compounds. For the magnetic moment of  $R$  atoms, experimental values are also varied. The calculated value of  $m_{\text{Tb}} = 9.23 \mu_B/\text{Tb}$  is nearly identical to the very recent experimental value measured by Mielke and co-workers [41] at 2 K. The calculated  $m_{\text{Dy}}$  also agrees well with neutron diffraction measurements [15, 20, 41]. For other  $R$  elements, the calculated  $m_R$  values are generally larger than reported experimental ones. Ho in  $\text{HoMn}_6\text{Sn}_6$  has the largest difference between the calculated and experimental values, 10.14 and 8.43  $\mu_B/\text{Ho}$ , respectively. However, Clatterbuck *et al.* [22] estimated the net magnetic moment of  $\text{HoMn}_6\text{Sn}_6$  from the magnetization curve at 10 K and obtained 3.26  $\mu_B/\text{f.u.}$ , agreeing fairly well with the calculated value of 3.0  $\mu_B/\text{f.u.}$  Furthermore, larger experimental Ho moment measured by the neutron diffraction had been reported in doped  $\text{HoMn}_6\text{Sn}_6$  compounds [29], e.g., with  $m_{\text{Ho}} = 9.53 \mu_B$  in  $\text{HoMn}_6\text{Sn}_5\text{In}$ . The difference between the experiments and theory may be relevant to the easy-cone orientation and the fact that we also partition magnetization into interstitial and Sn sites, which are AFM aligned with Mn.

#### B. Intersublattice $R$ -Mn exchange coupling

The inter-sublattice magnetic couplings between  $R$  and Mn sublattice play an essential role in aligning the FM

Mn-bilayers and stabilizing long-range Mn ordering. It also affects  $T_{\text{SR}}$  as a larger  $J$  suppresses the thermal acti-

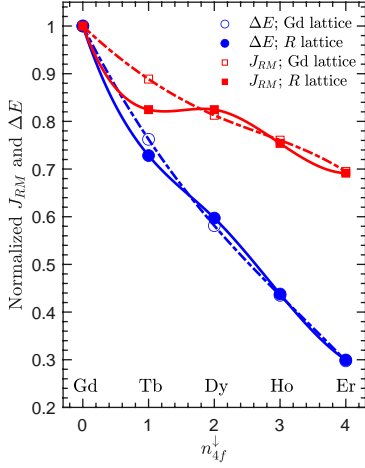


FIG. 2. Inter-sublattice  $R$ -Mn exchange coupling parameter  $J$  and magnetic energy  $\Delta E$  as functions of the electron occupancy in  $R$ - $4f$  minority spin channel  $n_{4f}^{\downarrow}$  in  $RMn_6Sn_6$  with  $R = \text{Gd, Tb, Dy, Ho, and Er}$ .  $\Delta E = E_{\text{AFM}} - E_{\text{FM}}$  is calculated as the energy difference between the AFM and FM spin configurations of  $R$  and Mn sublattices. To separate the structural and chemical effects, calculations using the lattice parameters of  $\text{GdMn}_6\text{Sn}_6$  are also carried out and denoted as open squares and circles.

vation of  $4f$  electrons into excited multiplet, which makes the thermal average of the  $4f$  charge cloud more spherical and isotropic. We estimate the  $R$ -Mn coupling  $J_{RM}$  by mapping the total energies of FM and FI  $R$ -Mn spin configurations into a Heisenberg model defined as

$$H_{RM} = \sum_{i \in R, j \in \text{Mn}} J_{RM} S_i \cdot S_j \quad (6)$$

Here,  $S_i = m_i^s/2$  and  $m_i^s$  is the spin magnetic moment on site  $i$ . A positive  $J_{RM}$  corresponds to the AFM  $R$ -Mn coupling.

Figure 2 show the  $R$ -Mn magnetic energy  $\Delta E$  and exchange parameter  $J_{RM}$ , normalized with respect to the values of  $\text{GdMn}_6\text{Sn}_6$ , as functions of the electron occupancy in the minority  $R$ - $4f$  spin channel [42]. The magnetic interaction energy  $\Delta E = E_{\text{AFM}} - E_{\text{FM}}$  is calculated as the energy difference between the AFM and FM spin configurations of  $R$  and Mn sublattices. To separate the chemical and structural effects, we also perform the calculations for all  $RMn_6Sn_6$  compounds using the lattice parameters of  $\text{GdMn}_6\text{Sn}_6$ . The  $R$ -Mn intersublattice couplings are AFM for all  $R$  elements, consistent with experiments. The corresponding magnetic energy  $\Delta E$  and exchange parameter  $J_{RM}$  decrease by  $\sim 70\%$  and  $\sim 30\%$ , respectively, when  $R$  goes from Gd to Er. The abnormality of  $J_{RM}$  at  $R = \text{Tb}$  is related to the structural change considering calculations that use the Gd lattice parameters give a smooth curve, as shown in Figure 2.

Besides the decrease of  $R$  spin moment, the reduction of  $R$ -Mn exchange energy from Gd to Er is caused by the weakening of exchange-coupling parameter  $J_{RM}$ . A similar decreasing of  $J_{RM}$  has also been observed in other

rare-earth transition-metal alloys, especially pronounced in light rare-earth series [43–45]. However, the mechanism behind the decreasing  $J_{RM}$  is not apparent; one may assume that  $J_{RM}$  remains the same considering the similarities of band structures throughout the series. The exchange coupling between  $R$ - $4f$  spin and Mn- $3d$  spin are primarily through the  $R$ - $5d$  electrons. The decrease of  $J_{RM}$  with increasing atomic number had been ascribed to the lanthanide contraction, which reduces the overlap between  $4f$  and  $5d$  charge densities [46, 47]. The change of lattice parameters can also affect the  $4f$ - $5d$  overlap and  $5d$ - $3d$  hybridization, affecting the  $J_{RM}$ , as shown in the abnormality of  $J_{RM}$  at  $R = \text{Tb}$  in Fig. 2.

### C. Magnetocrystalline anisotropy: *ab initio*

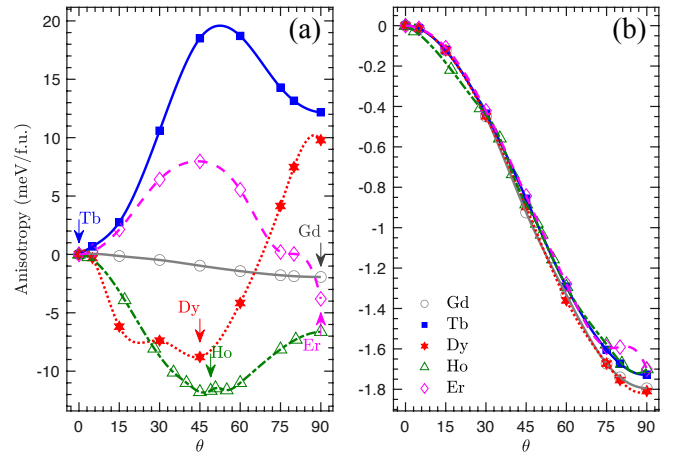


FIG. 3. Variation of magnetic energy (in meV/f.u.) as a function of spin-axis rotation in  $RMn_6Sn_6$ , with  $R = \text{Gd, Tb, Dy, Ho, and Er}$ , calculated (a) with and (b) without  $R$ - $4f$  contributions.  $\theta$  is the angle between the spin direction and the out-of-plane direction. The experimental easy directions for each compound are denoted by arrows in panel (a).

MA in  $RMn_6Sn_6$  consists of both contributions from  $R$  and Mn sublattices. They have different temperature dependence and dominate at lower temperatures and higher temperatures, respectively. MA becomes essential to maintain the long-range FM ordering in low-dimension materials or bulk materials consisting of magnetic layers that weakly coupled together, according to the Mermin-Wagner theorem [48, 49].

At lower temperatures, experiments found that  $\text{TbMn}_6\text{Sn}_6$  has easy-axis anisotropy and  $\text{ErMn}_6\text{Sn}_6$  has easy-plane anisotropy, while the  $\text{HoMn}_6\text{Sn}_6$  and  $\text{DyMn}_6\text{Sn}_6$  have an easy-cone anisotropy with the quantization axis along the  $\theta = 40\text{--}50^\circ$  directions. Figure 3(a) shows the calculated total energies as functions of spin-quantization direction, characterized by the angle  $\theta$  deviated from the  $c$  axis. The calculated easy directions for all five compounds agree well with experiments.  $\text{GdMn}_6\text{Sn}_6$  shows a cosine-like  $E(\theta)$  dependence, and the amplitude

is one order of magnitude smaller than other  $RMn_6Sn_6$  compounds. In contrast, all four other compounds show a non-monotonic dependence of  $E$  on the magnetic quantization direction  $\theta$ , suggesting substantial higher-order MAE constants.

At higher temperatures, experiments [15, 16, 20] found that all compounds have an easy spin axis within the basal plane, suggesting the Mn sublattice has easy-plane anisotropy. Here, we theoretically confirm the easy-plane contribution of Mn sublattice by calculating the MAE contributions from non-4*f* electrons. This is achieved by treating  $R$ -4*f* electrons in the open-core approach, in which spherical  $R$ -4*f* charges do not contribute to MAE. Figure 3(b) shows that Mn sublattices have easy-plane anisotropy as found in experiments. Unlike the total MAE, which contains the contribution from the  $R$  sublattice, the Mn MAE shows negligible higher-order terms as expected for non-4*f* elements. Moreover, remarkably, all compounds have a similar amplitude as calculated in  $GdMn_6Sn_6$ , much smaller than MAE induced by other  $R$  atoms. Overall, MAE is generally weaker than the  $R$ -Mn exchange coupling in  $RMn_6Sn_6$ . As a result, at lower temperatures, the easy direction is dictated by the  $R$  sublattice. Furthermore, it is worth noting that although we often associate the non-4*f* MAE contribution to the Mn sublattice, indeed, it is a combined effect of the Mn-3*d* spin polarization and the large Sn-4*p* SOC. This MA mechanism is rather general in many systems that consist of magnetic 3*d* atoms and heavier atoms, including permanent magnet FePt [34], topological materials  $MnBi_2Te_4$  [50], and magnetic 2D van der Waals materials  $CrI_3$  [51]. Ghimire *et al.* have revealed that the MA in  $YMn_6Sn_6$  consists of an easy-axis single-ion MA and a stronger easy-plane anisotropic exchange, resulting in an overall easy-plane MA [14].

The mechanism of the easy-cone axis in  $DyMn_6Sn_6$  and  $HoMn_6Sn_6$  is not well understood. For example, it has been argued that the easy-cone direction in  $HoMn_6Sn_6$  results from the competition between easy-plane Mn contribution and an easy-axis (weaker than those of Tb) from the Ho sublattice. However, considering the Mn sublattice contribution is much smaller than the total MAE, we argue that Dy and Ho MAE themselves prefer the easy direction off the  $z$ -axis. To verify, we turn off the SOC on Mn and Sn sites in  $HoMn_6Sn_6$  and find that the calculated easy direction remains the same. Thus, we conclude that the easy-cone axis results from the dominant Ho MAE itself instead of the competition between an easy-axis Ho MA and easy-plane Mn MA.

#### D. Rare-earth anisotropy: Crystal-field model

The dominant rare-earth contribution to the magnetocrystalline anisotropy reflects the crystal-field interaction of the 4*f* electrons. This interaction was first described in terms of electrostatic interaction in insulators [52], but the theory also applies to covalent solids and

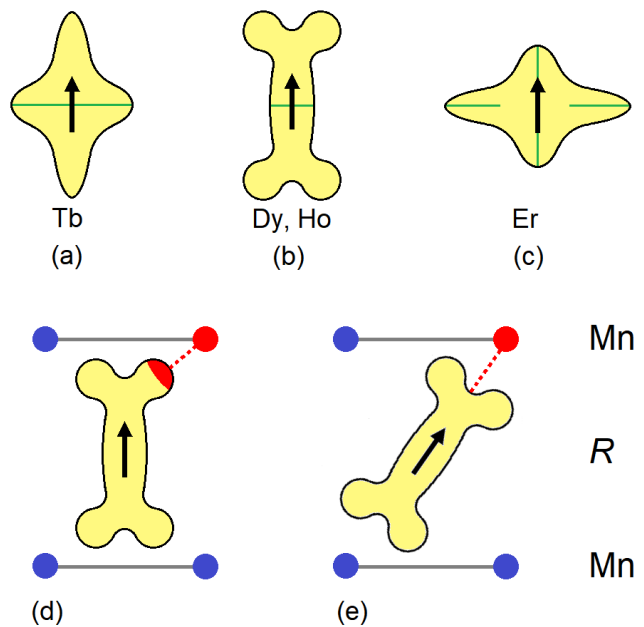


FIG. 4. Real-space origin of easy-cone magnetism in the present compounds: (a–c) schematic 4*f* electron clouds, (d) energetically unfavorable spin direction, and (e) energetically favorable spin direction. The quadrupole moment is negative in (a,b) and positive in (c), whereas the hexadecapole moment is positive in (a, c) and negative in (b).

metals, where it is often called ligand-field theory [53, 54]. Up to 4th order, the CF interaction of hexagonal crystals is described by the CFP  $A_2^0$  and  $A_4^0$  [39, 52, 53, 55, 56]. The anisotropy energy is, up to 4th order,

$$E_a = K_1 \sin^2(\theta) + K_2 \sin^4(\theta), \quad (7)$$

where

$$K_1 = -\frac{3}{2} A_2^0 Q_2 - 5 A_4^0 Q_4, \quad (8)$$

$$K_2 = \frac{35}{8} A_4^0 Q_4. \quad (9)$$

In these equations, the  $Q_m$  are the electrostatic multipole moments of the rare-earth 4*f* shells; quadrupole moment  $Q_2 = a_J \langle r^2 \rangle_{4f} \mathcal{O}_2^0$  and hexadecapole moment  $Q_4 = b_J \langle r^4 \rangle_{4f} \mathcal{O}_4^0$ . Here, the Stevens coefficients  $a_J$  and  $b_J$ , the operator equivalents  $\mathcal{O}_m^0$ , and the rare-earth radii  $\langle r^l \rangle_{4f}$  are well-known [55, 57], and low-temperature values of  $Q_2$  and  $Q_4$  have been tabulated in Ref. [56].

In isostructural compounds,  $A_2^0$  and  $A_4^0$  exhibit little change across the lanthanide series, because they reflect the crystalline environment of the rare-earth atoms. The striking differences in Fig. 3(a) reflect the multipole moments. Physically, the strong spin-orbit interaction of the rare earths yields a rigid coupling between the spin and the orbital moments of  $R$  atom, so that the magnetic anisotropy is determined by the electrostatic interaction of the  $R$ -4*f* charge clouds with the crystalline environment [39, 56]. The charge distribution of the Gd-4*f*



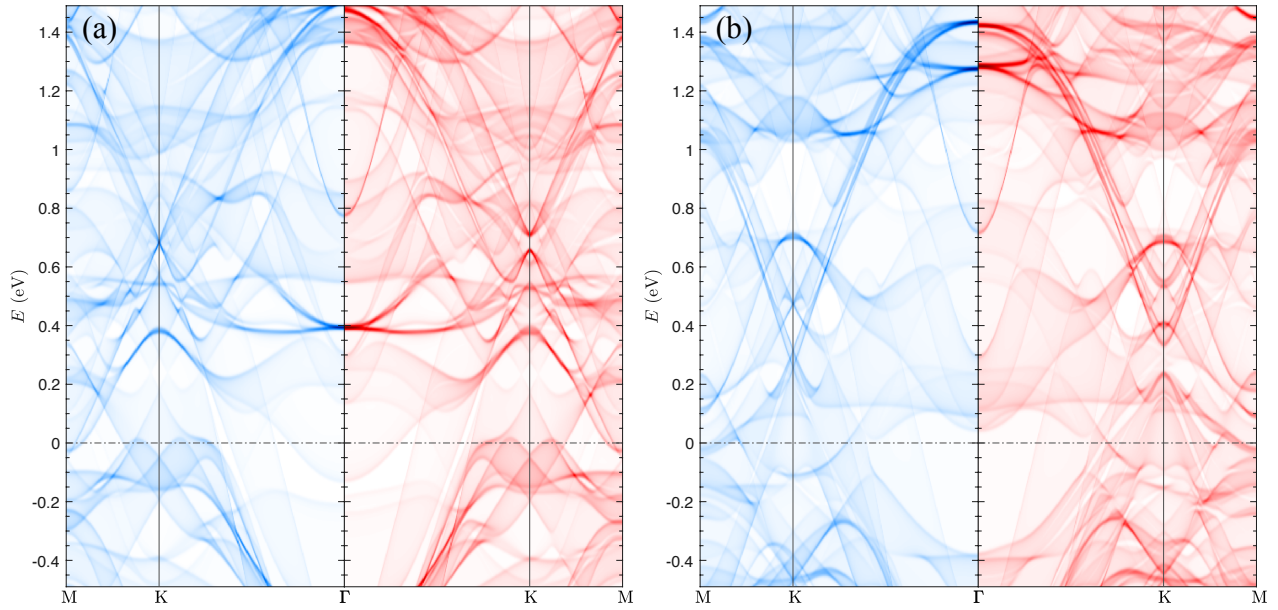


FIG. 5. Band structures projected on surface BZ calculated without (blue) and with (red) SOC in  $\text{TbMn}_6\text{Sn}_6$ . The  $k$ -dependent DOS are integrated along  $k_z$  (see Eq. (10)) and are calculated in (a) DFT and (b) DFT+ $U$ . Hubbard  $U = 2.5$  eV and Hund's rule coupling  $J = 0.7$  eV are applied on Mn-3d orbitals, and the AMF double-counting scheme is employed in DFT+ $U$ .

electrons is spherical (half-filled  $4f$  shell), but the other lanthanides have aspherical charge distributions and exhibit nonzero anisotropy contributions. This asphericity provides a qualitative explanation of the curves in Fig. 3(a). Lowest-order interactions ( $Q_2$ ) determine the basic spin orientation (easy axis vs. easy plane), but to understand easy-cone behavior, one needs  $Q_4$  [39]. The  $R$  elements considered in this paper have  $Q_4 > 0$  (Tb, Er) and  $Q_4 < 0$  (Dy, Ho), as schematically shown in Figs. 4(a)–4(c). Crystal-field charges in both metals and nonmetals are usually negative [54, 56], so that the Mn coordination of the  $R$  atoms in  $\text{RMn}_6\text{Sn}_6$  (about  $50^\circ$ ) yields a negative  $A_4^0$  and realizes the situation outlined in Figs. 4(d) and 4(e). In a nutshell, the combination of  $Q_2$  and  $Q_4$  creates a bone-like  $4f$  charge distribution, and the electrostatic repulsion between the crystal-field charges (Mn) and the negatively charged  $4f$  electrons causes the magnetization direction to deviate from the  $c$ -axis. In Figs. 4(d) and 4(e) this repulsion is exemplified by dashed red lines nearby red-colored regions.

Both the calculated MAE and the extracted CFP are very high, comparable to that of  $\text{SmCo}_5$ . Published experimental evidence [16], especially the high anisotropy fields implicit Fig. 9 therein, is consistent with the present prediction. Moreover, recently, using inelastic neutron scattering (INS) measurement, Riberolles *et al.* have estimated the magnetic anisotropy strength in  $\text{TbMn}_6\text{Sn}_6$  [58]. The INS-deduced single-ion Tb anisotropy,  $K_{\text{Tb}}(S_{\text{Tb}}^z)^2$ , is one order of magnitude larger than that of Mn, comparable to present *ab initio* prediction. On the other hand, INS suggested that the Mn

sublattice has an easy-axis single-ion anisotropy instead of the calculated easy-plane MAE. Further experimental and theoretical efforts are required to resolve this discrepancy.

Note that rare-earth anisotropy constants of order  $n > 2$  are normally much smaller than second-order anisotropy constants [56], which explains the relatively rare overall occurrence of easy-cone magnetism. In the present system, the high fourth-order anisotropy is a unique consequence of the Mn-coordination of the rare-earth atoms in the structure, which have 12 nearby Mn atoms in adjacent planes. CFP are proportional to the number of neighbors, each contributing an intrinsic crystal-field contribution  $A'_n$ , and these intrinsic contributions are multiplied by coordination factors [54, 56]. For  $A_4^0$ , the coordination factor is  $P_4(\cos\theta) = (35\cos^4(\theta) - 30\cos^2(\theta) + 3)/8$ , which has an extreme of  $-0.429$  at  $49.1^\circ$ .

The above simplistic crystal-field model provides an intuitive understanding of the the easy directions in  $\text{RMn}_6\text{Sn}_6$ . More comprehensive *ab initio* calculations of crystal field parameters, although challenging, could be useful to quantify the roles of Sn and Mn ligand shells to CFP and MAE constants, including the sixth-order terms.

#### IV. RESULTS ON BAND TOPOLOGY: EFFECTS OF MAGNETISM, ELECTRON CORRELATION, AND SURFACE

### A. Dirac crossings and gap openings

In Chern-gapped insulators, edge states may significantly contribute to the transport properties by avoiding backscattering when  $E_F$  is located within the Chern gap.  $\text{TbMn}_6\text{Sn}_6$  is metallic and the band structures [1] calculated in DFT found that a 2D-like (weak  $k_z$ -dependent) Chern-gapped Dirac crossing, mainly consists of Mn in-plane orbitals, occurring slightly above  $E_F$ . Here, we systematically investigate how the band structures near the Fermi level in  $\text{RMn}_6\text{Sn}_6$  evolve with  $R$ , electron correlations, and spin reorientation.

Near the Fermi energy, all five compounds share similar band structures, as the non- $4f$  electrons dominate them. Multiple DCs occur at the  $K$ -point near  $E_F$ , below or above  $E_F$ , as expected from the kagome Mn lattice. SOC splits the crossings and opens gaps of various sizes at BZ corners with spin along the  $z$  direction. However, most of them strongly depend on the  $k_z$  value, reflecting the 3D nature of the corresponding bands. To better illustrate the  $k_z$  dependence of band structures, we project all bands on the surface BZ by integrating the  $k$ -dependent DOS,  $D(\mathbf{k}_\parallel, k_z, \omega)$ , over  $k_z$ ,

$$I(\mathbf{k}_\parallel, \omega) = \int_0^1 dk_z \sum_i \delta[\omega - E_i(\mathbf{k}_\parallel, k_z)]. \quad (10)$$

Here,  $k_z$  is integrated from 0 to 1 r.l.u., while  $\mathbf{k}_\parallel$  is along the in-plane path  $\Gamma$ - $K$ - $M$ .

Figure 5(a) compares the projected  $\text{TbMn}_6\text{Sn}_6$  bands calculated without and with SOC in DFT, shown as blue and red bands, respectively. Two occupied DCs occur at  $\sim 0.05$  and  $\sim 0.2$  eV below  $E_F$ , respectively, whose gaps are barely opened by SOC. The most prominent  $k_z$ -independent DC lies  $\sim 0.7$  eV above  $E_F$ , dominated by the Mn- $d$  characters (see Table S1). In contrast to the two occupied DCs, a much larger gap is induced at this DC when SOC is included, agreeing with the previous report [1]. The gap size depends on the band characters at these DCs and how effectively SOC can couple them. Other  $\text{RMn}_6\text{Sn}_6$  compounds show overall similar band structures (see Fig. S1).

### B. Effects of Mn- $3d$ electron correlation

Note that the position of this Dirac crossing is much higher than the previously reported value of  $\sim 0.15$  eV above  $E_F$  (see Extended Data Fig. 9 in Ref. [1]), and is unlikely to play a significant role in transport properties. On the other hand, it is unclear whether the plain DFT treatment of Mn sublattice in  $\text{RMn}_6\text{Sn}_6$  is sufficient. Indeed, for example, a sizable Hubbard  $U = 4$  eV had been applied on Mn- $3d$  orbitals in DFT+DMFT to describe the measured band structure in  $\text{YMn}_6\text{Sn}_6$  [9], while most of other studies treated Mn within DFT [1]. Applying additional electron repulsion on Mn- $3d$  orbitals

affects their energetics—the position of the corresponding bands and DCs. Thus, here, we explore the effects of Mn- $d$  electron correlations on the band structures near  $E_F$  within DFT+ $U$ .

Hubbard  $U$  is applied on Mn- $3d$  orbitals in DFT+ $U$  using both FLL and AMF double-counting schemes. Within the FLL scheme, the Mn magnetic moment quickly increases to  $\sim 3.3\mu_B/\text{Mn}$  at  $U = 1$  eV, overestimating the experimental value of  $2.4\mu_B/\text{Mn}$ . In contrast, within the AMF scheme, the calculated Mn moment remains close to the experimental value in the range of  $U = 0$ – $2.5$  eV till further increasing  $U$  decreases Mn moment. Indeed, compared to the FLL scheme, the AMF scheme is generally more suitable for the less strongly correlated metallic systems. Therefore, here we only present band structures calculated using AMF scheme.

Figure 5(b) shows the band structures calculated with  $U_{\text{Mn}} = 2.5$  eV and  $J_{\text{Mn}} = 0.7$  eV, showing a SOC-gapped DC located at  $\sim 0.2$  eV above  $E_F$ . Interestingly, the gap size is even larger than the one obtained in DFT, and the flat band near the 0.55 eV obtained in DFT is also lowered to 0.1 eV in DFT+ $U$ . The on-site Mn moment decreases to  $2.2\mu_B/\text{Mn}$ . Thus, additional correlation effects on Mn- $3d$  orbitals can profoundly affect topological band structures near  $E_F$  in these systems and are worth further investigation.

However, in general, the choice of the correlated orbitals and the associated on-site  $U$  and  $J$  are not well-defined for metallic systems. Moreover, off-site nonlocal exchange correlations can also play important roles [59, 60]. Thus, the comparison with ARPES results may be useful to determine the best  $U$  and  $J$  parameters. On the theoretical side, parameter-free method investigation of electron correlation effects [59–61] on electronic structures and magnetic properties could also be useful.

### C. Effects of spin orientation

It is well known that Kagome materials in the presence of SOC and out-of-plane magnetization effectively realize the Haldane model for a Chern insulator without Landau levels [1–3, 62]. This model describes spin-polarized electrons hopping in a background of staggered magnetic fluxes on a lattice that supports Dirac crossings in the absence of the magnetic field. In  $\text{RMn}_6\text{Sn}_6$ , the bands that are mostly localized in the Mn Kagome layer naturally experience DCs at the  $K$  and  $K'$  points near  $E_F$ , as shown in Fig. 6. Due to FM order, these DCs occur within the same spin channel, which can be Chern gapped by intrinsic SOC (see Eq. (2)). Besides the itinerant band character, e.g., the  $d$ -orbital characters of Mn atoms in the Kagome lattice, the size of the SOC-induced gaps also depend on the spin orientations of magnetic Mn atoms, which can evolve with the  $R$  element type and with temperature [63]. Temperature- and substitution-induced spin reorientations thus have direct consequences on topological transport properties such as the quantum



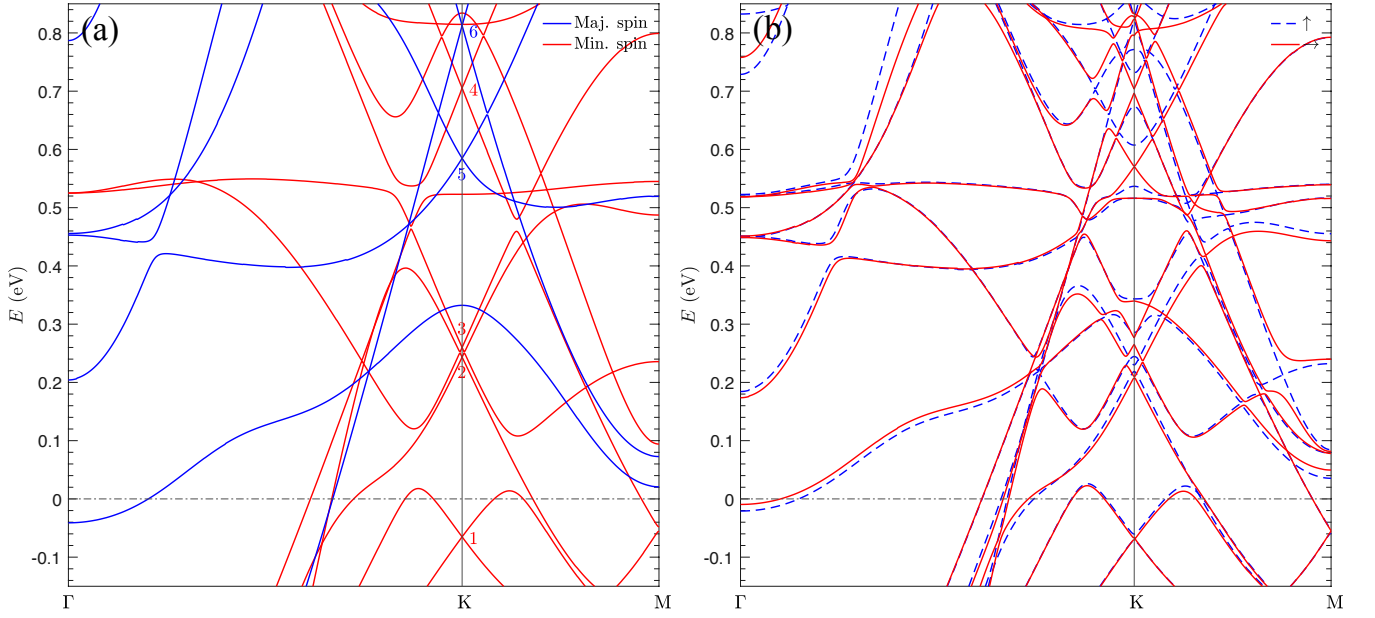


FIG. 6. Band structure near  $E_F$  in  $\text{HoMn}_6\text{Sn}_6$  calculated (a) without SOC and (b) with SOC. In panel (a), the majority-spin and minority-spin, referred to Mn site, are in blue and red, respectively. In panel (b), the band structures are calculated with the spin-quantization axis along the out-of-plane (blue dashed line) and in-plane (red solid line) directions. Both magnetic sublattices are ordered. The gap sizes depend on spin orientations.

anomalous Hall conductivity, if these (gapped) crossings occur close to the Fermi energy.

For example, the gap size should vary when  $\text{RMn}_6\text{Sn}_6$  goes from the easy-axis  $\text{TbMn}_6\text{Sn}_6$  to easy-cone  $\text{HoMn}_6\text{Sn}_6$  or when  $\text{RMn}_6\text{Sn}_6$  is heated above the spin-reorientation temperatures. Figures 6(a) and 6(b) show the band structures in  $\text{HoMn}_6\text{Sn}_6$  calculated without and with SOC, respectively. For the simplicity of illustration, here we focus on the large gap of the DC at 0.7 eV, labeled as DC4 in Fig. 6(a). Figure 6(b) shows the gap almost vanishes when the spin-quantization axis rotates from the out-of-plane direction to the in-plane direction. This can be understood by starting from the non-SOC band structures and treat SOC within perturbation theory.

DC4 mainly consists of  $|m = \pm 2\rangle$  and  $|m = 0\rangle$  Mn-3d characters (see Table S1) in the minority spin channel.

Since the DCs occur within the same spin channel, the gap size  $\Delta$  is proportional to the spin-parallel part of  $H_{\text{so}}$ , as shown in Eq. (2), and can be written as

$$\Delta \propto L_z \cos(\theta) + f(L_+, L_-, \theta, \varphi). \quad (11)$$

The second term in Eq. (11) vanishes because  $L_{\pm}$  do not couple between  $|m = \pm 2\rangle$  and  $|m = 0\rangle$  states [40]. Thus, the gap size is solely determined by  $L_z \cos(\theta)$ , which vanishes at  $\theta = 90^\circ$  with the in-plane spin orientations.

The band characters of other DCs may consist of orbitals that can also be coupled by  $L_{\pm}$ . The corresponding SOC-induced gap can remain open when spin is in-plane. Moreover, DCs contains a larger Sn component can have a larger gap, as Sn has a much larger SOC constant than Mn. Finally, when DCs are next to each other, multiple DCs can be coupled by SOC, complicating the analysis.

#### D. Surface effects on magnetism and bandstructure

Finally, we investigate the surface effects on the magnetism and electronic structures in  $\text{RMn}_6\text{Sn}_6$ . Experimentally, purely Mn Kagome lattices without detectable defects have been observed over a large field of view [1] in  $\text{TbMn}_6\text{Sn}_6$ . Here, we calculate the electronic structures in monolayer and bilayer  $\text{TbMn}_6\text{Sn}_6$  with terminating Mn surface on one side and  $R$ -Sn surface on the other side. Each layer is one f.u. thick, as shown in Fig. 1, and contains two Mn Kagome planes. Sufficiently large

vacuum space is used in the unit cell to avoid the interaction between neighboring slabs due to periodic boundary conditions. The structure is relaxed so that the force on each atom is less than 1 mRy/a.u.

Both monolayer and bilayer  $\text{TbMn}_6\text{Sn}_6$  remain metallic as in bulk. The Tb atom on the surface has a slightly larger moment. For example, in a bilayer system, the magnetic moment of the Tb atom is 6.29 (6.35)  $\mu_B/\text{Tb}$  for the surface (subsurface) atom. In contrast, remarkably, the surface Mn atoms have much larger magnetic moments and stronger exchange splittings than in the

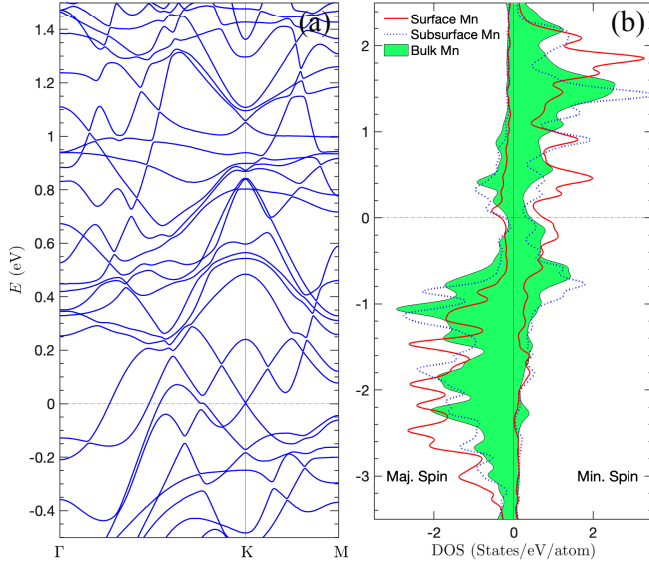


FIG. 7. (a) Band structures and (b) partial density of states projected on the surface (red solid line) and subsurface (blue dashed line) Mn sites in monolayer  $\text{TbMn}_6\text{Sn}_6$ . In panel (b), bulk Mn (green filled area) DOS is also shown to compare.

bulk case. For both monolayer and bilayer cases, Mn atoms on the terminating surface have a magnetic moment of  $3.3 \mu_B/\text{Mn}$ , while the subsurface Mn layers have a similar moment of  $\sim 2.4 \mu_B/\text{Mn}$  as in the bulk case. As a result, near the Fermi level, the spin splitting of the surface Mn states increases. Figure 7 shows the band structures, and partial density of states projected on surface and subsurface Mn layers in monolayer  $\text{TbMn}_6\text{Sn}_6$ . The band structures change profoundly compared to the bulk band, and interestingly, a DC occurs at  $K$  at  $E_F$ . A larger spin splitting for the surface Mn states, induced by their larger moments, are shown in Fig. 7(b). Overall,  $\text{RMn}_6\text{Sn}_6$  is quite different from 2D van der Waals materials, where the calculated on-site moment and intralayer magnetic couplings remain similar in bulk and monolayer forms [51].

## V. CONCLUSIONS

In summary, we have systematically investigated the electronic structures and intrinsic magnetic properties of  $\text{RMn}_6\text{Sn}_6$  for  $R = \text{Gd}, \text{Tb}, \text{Dy}, \text{Ho}, \text{and Er}$ . In particular, we revealed a non-monotonic dependence of the magnetic energy  $E$  on the magnetic quantization axis  $\theta$  for all compounds except  $\text{GdMn}_6\text{Sn}_6$ , suggesting the importance of higher-order MAE parameters. Our calculations show that  $\text{TbMn}_6\text{Sn}_6$  has an easy-axis,  $\text{GdMn}_6\text{Sn}_6$  and  $\text{ErMn}_6\text{Sn}_6$  have an easy-plane anisotropy, while

$\text{DyMn}_6\text{Sn}_6$  and  $\text{HoMn}_6\text{Sn}_6$  have easy-cone anisotropy with the easy axis deviating from the  $c$  axis by  $\theta = 45^\circ$  and  $49^\circ$ , respectively. All these results agree well with experimental observations. We further demonstrated that the easy-cone anisotropy in  $\text{DyMn}_6\text{Sn}_6$  and  $\text{HoMn}_6\text{Sn}_6$  results from the dominant  $R$  MA itself instead of the competition between an easy-axis  $R$  MA and the easy-plane Mn MA.

We have further investigated the band structures in  $\text{RMn}_6\text{Sn}_6$  and how Dirac crossings and SOC-induced gaps evolve with the type of  $R$  atom, additional electron correlations, and spin reorientation. In the plain DFT treatment of the Mn sublattice, the most prominent SOC-gapped 2D-like DC is located at about 0.7 eV above  $E_F$ . Including additional electron correlation of Mn- $d$  orbitals beyond DFT, however, impacts the positions of DCs near  $E_F$ , and prominently lowers the SOC-gapped DC closer to  $E_F$ . Thus, although the MAE can be well described already in the plain DFT treatment of the Mn sublattice, other properties, such as transport properties and exchange couplings, could be more sensitive to the detailed band structures near  $E_F$ . Future experiments such as ARPES may be helpful to calibrate or validate the strength of electron repulsion on the Mn kagome lattice. On the theoretical side, parameter-free method investigations on electronic structures and electron correlations in  $\text{RMn}_6\text{Sn}_6$  could also be helpful.

Finally, unlike 2D van der Waals materials, we observe that in  $\text{RMn}_6\text{Sn}_6$  the Mn moments on the terminating Mn Kagome surface can have a much larger moment of  $3.3 \mu_B/\text{Mn}$ , and correspondingly an enhanced exchange splitting that accompanies the shifting of Dirac crossings near  $E_F$ . Such predicted enhancement of the surface Mn moment remains to be confirmed experimentally.

## ACKNOWLEDGMENTS

The authors gratefully acknowledge discussions with Q. Niu. Y. L. and L. K. are supported by the U.S. Department of Energy, Office of Science, Office of Basic Energy Sciences, Materials Sciences and Engineering Division, and Early Career Research Program. R. J. M. and P. P. O. are supported by the U.S. Department of Energy, Office of Basic Energy Sciences, Division of Materials Sciences and Engineering. Ames Laboratory is operated for the U.S. Department of Energy by Iowa State University under Contract No. DE-AC02-07CH11358. The work in Nebraska is supported by the National Science Foundation/EPSCoR RII Track-1: Emergent Quantum Materials and Technologies (EQUATE), Award OIA-2044049. This research used resources of the National Energy Research Scientific Computing Center (NERSC), a U.S. Department of Energy Office of Science User Facility operated under Contract No. DE-AC02-05CH11231.

- 
- [1] J.-X. Yin, W. Ma, T. A. Cochran, X. Xu, S. S. Zhang, H.-J. Tien, N. Shumiya, G. Cheng, K. Jiang, B. Lian, *et al.*, Quantum-limit Chern topological magnetism in  $\text{TbMn}_6\text{Sn}_6$ , *Nature* **583**, 533 (2020).
- [2] G. Xu, B. Lian, and S.-C. Zhang, Intrinsic quantum anomalous hall effect in the kagome lattice  $\text{Cs}_2\text{limn}_3\text{f}_{12}$ , *Phys. Rev. Lett.* **115**, 186802 (2015).
- [3] E. Tang, J.-W. Mei, and X.-G. Wen, High-temperature fractional quantum hall states, *Phys. Rev. Lett.* **106**, 236802 (2011).
- [4] T. Neupert, L. Santos, C. Chamon, and C. Mudry, Fractional quantum hall states at zero magnetic field, *Phys. Rev. Lett.* **106**, 236804 (2011).
- [5] W. Ma, X. Xu, J.-X. Yin, H. Yang, H. Zhou, Z.-J. Cheng, Y. Huang, Z. Qu, F. Wang, M. Z. Hasan, and S. Jia, Rare Earth Engineering in  $\text{RMn}_6\text{Sn}_6$  ( $R = \text{Gd-Tm, Lu}$ ) Topological Kagome Magnets, *Phys. Rev. Lett.* **126**, 246602 (2021).
- [6] Z. Liu, N. Zhao, M. Li, Q. Yin, Q. Wang, Z. Liu, D. Shen, Y. Huang, H. Lei, K. Liu, and S. Wang, Electronic correlation effects in the kagome magnet  $\text{gdmn}_6\text{sn}_6$ , *Phys. Rev. B* **104**, 115122 (2021).
- [7] X. Xu, J.-X. Yin, W. Ma, H.-R. Tian, X.-B. Qiang, H. Zhou, J. Shen, H. Lu, T.-R. Chang, Z. Qu, and S. Jia, Topological charge-entropy scaling in kagome chern magnet  $\text{tbmn}_6\text{sn}_6$  (2021), arXiv:2110.07563 [cond-mat.str-el].
- [8] L. Gao, S. Shen, Q. Wang, W. Shi, Y. Zhao, C. Li, W. Cao, C. Pei, J.-Y. Ge, G. Li, J. Li, Y. Chen, S. Yan, and Y. Qi, Anomalous hall effect in ferrimagnetic metal  $\text{rmn}_6\text{sn}_6$  ( $r = \text{tb, dy, ho}$ ) with clean mn kagome lattice, *Applied Physics Letters* **119**, 092405 (2021).
- [9] M. Li, Q. Wang, G. Wang, Z. Yuan, W. Song, R. Lou, Z. Liu, Y. Huang, Z. Liu, H. Lei, Z. Yin, and S. Wang, Dirac cone, flat band and saddle point in kagome magnet  $\text{ymn}_6\text{sn}_6$ , *Nature Communications* **12**, 3129 (2021).
- [10] W. Ma, X. Xu, Z. Wang, H. Zhou, M. Marshall, Z. Qu, W. Xie, and S. Jia, Anomalous hall effect in the distorted kagome magnets  $(\text{nd,sm})\text{mn}_6\text{sn}_6$ , *Phys. Rev. B* **103**, 235109 (2021).
- [11] T. Asaba, S. M. Thomas, M. Curtis, J. D. Thompson, E. D. Bauer, and F. Ronning, Anomalous hall effect in the kagome ferrimagnet  $\text{gdmn}_6\text{sn}_6$ , *Phys. Rev. B* **101**, 174415 (2020).
- [12] Q. Wang, K. J. Neubauer, C. Duan, Q. Yin, S. Fujitsu, H. Hosono, F. Ye, R. Zhang, S. Chi, K. Krycka, H. Lei, and P. Dai, Field-induced topological hall effect and double-fan spin structure with a  $c$ -axis component in the metallic kagome antiferromagnetic compound  $\text{Ymn}_6\text{sn}_6$ , *Phys. Rev. B* **103**, 014416 (2021).
- [13] R. L. Dally, J. W. Lynn, N. J. Ghimire, D. Michel, P. Siegfried, and I. I. Mazin, Chiral properties of the zero-field spiral state and field-induced magnetic phases of the itinerant kagome metal  $\text{ymn}_6\text{sn}_6$ , *Phys. Rev. B* **103**, 094413 (2021).
- [14] N. J. Ghimire, R. L. Dally, L. Poudel, D. C. Jones, D. Michel, N. T. Magar, M. Bleuel, M. A. McGuire, J. S. Jiang, J. F. Mitchell, J. W. Lynn, and I. I. Mazin, Competing magnetic phases and fluctuation-driven scalar spin chirality in the kagome metal  $\text{ymn}_6\text{sn}_6$ , *Science Advances* **6**, eabe2680 (2020).
- [15] B. El Idrissi, G. Venturini, B. Malaman, and D. Fruchart, Magnetic structures of  $\text{TbMn}_6\text{Sn}_6$  and  $\text{HoMn}_6\text{Sn}_6$  compounds from neutron diffraction study, *Journal of the Less Common Metals* **175**, 143 (1991).
- [16] G. Venturini, B. E. Idrissi, and B. Malaman, Magnetic properties of  $\text{RMn}_6\text{Sn}_6$  ( $R = \text{Sc, Y, Gd-Tm, Lu}$ ) compounds with  $\text{HfFe}_6\text{Ge}_6$ -type structure, *Journal of Magnetism and Magnetic Materials* **94**, 35 (1991).
- [17] G. Venturini, B. Chafik El Idrissi, E. Ressouche, and B. Malaman, Magnetic structure of  $\text{TbMn}_6\text{Ge}_6$  from neutron diffraction study, *Journal of Alloys and Compounds* **216**, 243 (1995).
- [18] J. Hu, K.-Y. Wang, B.-P. Hu, Y.-Z. Wang, Z. Wang, F. Yang, N. Tang, R. Zhao, and W. Qin, Magnetic transition and coercivity in  $\text{TbMn}_6\text{Sn}_6$ , *Journal of Physics: Condensed Matter* **7**, 889 (1995).
- [19] S. Kimura, A. Matsuo, S. Yoshii, K. Kindo, L. Zhang, E. Brück, K. Buschow, F. de Boer, C. Lefèvre, and G. Venturini, High-field magnetization of  $\text{RMn}_6\text{Sn}_6$  compounds with  $R = \text{Gd, Tb, Dy}$  and  $\text{Ho}$ , *Journal of Alloys and Compounds* **408-412**, 169 (2006), proceedings of Rare Earths'04 in Nara, Japan.
- [20] B. Malaman, G. Venturini, R. Welter, J. Sanchez, P. Vullet, and E. Ressouche, Magnetic properties of  $\text{RMn}_6\text{Sn}_6$  ( $R = \text{Gd-Er}$ ) compounds from neutron diffraction and Mössbauer measurements, *Journal of Magnetism and Magnetic Materials* **202**, 519 (1999).
- [21] N. K. Zaikov, A. N. Pirogov, N. V. Mushnikov, A. E. Teplykh, É. Z. Valiev, and Y. A. Dorofeev, Magnetic-field-induced spin-reorientational transition in  $\text{TbMn}_6\text{Sn}_6$ , *Journal of Experimental and Theoretical Physics Letters* **72**, 436 (2000).
- [22] D. Clatterbuck and K. Gschneidner, Magnetic properties of  $\text{RMn}_6\text{Sn}_6$  ( $R = \text{Tb, Ho, Er, Tm, Lu}$ ) single crystals, *Journal of Magnetism and Magnetic Materials* **207**, 78 (1999).
- [23] S. Tabatabai Yazdi, N. Tajabor, M. Rezaee Roknabadi, M. Behdani, and F. Pourarian, Magnetoelastic properties of  $\text{ErMn}_6\text{Sn}_6$  intermetallic compound, *Journal of Magnetism and Magnetic Materials* **324**, 723 (2012).
- [24] J.-l. Yao, S.-y. Zhang, B.-d. Liu, B.-g. Shen, R.-w. Wang, L.-g. Zhang, D.-r. Yang, and M. Yan, Unusual magnetic and transport properties of layered compound  $\text{ermn}_6\text{sn}_6$ , *Journal of Applied Physics* **95**, 7061 (2004).
- [25] J. Hu, F. Yang, Y. Wang, J. Wang, and F. R. de Boer, Metamagnetic Transition in  $\text{ErMn}_6\text{Sn}_6$ , *physica status solidi (b)* **214**, 135 (1999).
- [26] M. Dirken, R. Thiel, J. Brabers, F. de Boer, and K. Buschow, 155Gd mössbauer effect and magnetic properties of  $\text{GdMn}_6\text{Sn}_6$ , *Journal of Alloys and Compounds* **177**, L11 (1991).
- [27] G. Venturini, R. Welter, B. Malaman, and E. Ressouche, Magnetic structure of  $\text{Ymn}_6\text{Ge}_6$  and room temperature magnetic structure of  $\text{LuMn}_6\text{Sn}_6$  obtained from neutron diffraction study, *Journal of Alloys and Compounds* **200**, 51 (1993).
- [28] G. Venturini, D. Fruchart, and B. Malaman, Incommensurate magnetic structures of  $\text{RMn}_6\text{Sn}_6$  ( $R = \text{Sc, Y, Lu}$ ) compounds from neutron diffraction study, *Journal of Alloys and Compounds* **236**, 102 (1996).

- [29] C. Lefèvre, G. Venturini, and B. Malaman, Neutron diffraction study of the magnetocrystalline anisotropy in  $\text{TbMn}_6\text{Sn}_{5.8}\text{Ga}_{0.2}$ ,  $\text{TbMn}_6\text{Sn}_5\text{Ga}$ ,  $\text{HoMn}_6\text{Sn}_5\text{Ga}$  and  $\text{HoMn}_6\text{Sn}_5\text{In}$  compounds, *Journal of Alloys and Compounds* **358**, 29 (2003).
- [30] L. Ke, D. A. Kukusta, and D. D. Johnson, Origin of magnetic anisotropy in doped  $\text{Ce}_2\text{Co}_{17}$  alloys, *Phys. Rev. B* **94**, 144429 (2016).
- [31] L. Ke and D. D. Johnson, Intrinsic magnetic properties in  $R(\text{Fe}_{1-x}\text{Co}_x)_{11}\text{TiZ}$  ( $R=\text{Y}$  and  $\text{Ce}$ ;  $Z=\text{H}$ ,  $\text{C}$ , and  $\text{N}$ ), *Phys. Rev. B* **94**, 024423 (2016).
- [32] P. Blaha, K. Schwarz, G. K. H. Madsen, D. Kvasnicka, J. Luitz, R. Laskowski, F. Tran, and L. D. Marks, *WIEN2k: An Augmented Plane Wave plus Local Orbitals Program for Calculating Crystal Properties* (Vienna University of Technology, Austria, 2018).
- [33] J. P. Perdew, K. Burke, and M. Ernzerhof, Generalized Gradient Approximation Made Simple, *Phys. Rev. Lett.* **77**, 3865 (1996).
- [34] L. Ke, Intersublattice magnetocrystalline anisotropy using a realistic tight-binding method based on maximally localized Wannier functions, *Phys. Rev. B* **99**, 054418 (2019).
- [35] N. Marzari and D. Vanderbilt, Maximally localized generalized Wannier functions for composite energy bands, *Phys. Rev. B* **56**, 12847 (1997).
- [36] A. A. Mostofi, J. R. Yates, G. Pizzi, Y.-S. Lee, I. Souza, D. Vanderbilt, and N. Marzari, An updated version of wannier90: A tool for obtaining maximally-localised Wannier functions, *Computer Physics Communications* **185**, 2309 (2014).
- [37] I. Souza, N. Marzari, and D. Vanderbilt, Maximally localized Wannier functions for entangled energy bands, *Phys. Rev. B* **65**, 035109 (2001).
- [38] N. Marzari, A. A. Mostofi, J. R. Yates, I. Souza, and D. Vanderbilt, Maximally localized Wannier functions: Theory and applications, *Rev. Mod. Phys.* **84**, 1419 (2012).
- [39] R. Skomski, *Simple Models of Magnetism*, Oxford Graduate Texts (University Press, Oxford, 2008).
- [40] L. Ke and M. van Schilfgaarde, Band-filling effect on magnetic anisotropy using a Green's function method, *Phys. Rev. B* **92**, 014423 (2015).
- [41] C. Mielke III, W. Ma, V. Pomjakushin, O. Zaharko, X. Liu, J.-X. Yin, S. Tsirkin, T. Cochran, M. Medarde, V. Poree, *et al.*, Intriguing magnetism of the topological kagome magnet  $\text{TbMn}_6\text{Sn}_6$ , arXiv preprint arXiv:2101.05763 (2021).
- [42] J. Jensen and A. R. Mackintosh, *Rare earth magnetism* (Clarendon Press, Oxford, 1991).
- [43] R. Verhoef, P. Quang, J. Franse, and R. Radwański, The strength of the r-t exchange coupling in  $\text{r}_2\text{Fe}_{14}\text{b}$  compounds, *Journal of Magnetism and Magnetic Materials* **83**, 139 (1990).
- [44] J. Liu, F. de Boer, P. de Châtel, R. Coehoorn, and K. Buschow, On the 4f-3d exchange interaction in intermetallic compounds, *Journal of Magnetism and Magnetic Materials* **132**, 159 (1994).
- [45] N. Duc, T. Hien, D. Givord, J. Franse, and F. de Boer, Exchange interactions in rare earth-transition metal compounds, *Journal of Magnetism and Magnetic Materials* **124**, 305 (1993).
- [46] R. J. Radwański, The intersublattice molecular fields in the rare earth-cobalt intermetallics, *physica status solidi (b)* **137**, 487 (1986).
- [47] E. Belorizky, M. A. Fremy, J. P. Gavigan, D. Givord, and H. S. Li, Evidence in rare-earth (r)-transition metal (m) intermetallics for a systematic dependence of r-m exchange interactions on the nature of the r atom, *Journal of Applied Physics* **61**, 3971 (1987).
- [48] N. D. Mermin and H. Wagner, Absence of ferromagnetism or antiferromagnetism in one- or two-dimensional isotropic heisenberg models, *Phys. Rev. Lett.* **17**, 1133 (1966).
- [49] V. V. Mkhitarian and L. Ke, Self-consistently renormalized spin-wave theory of layered ferromagnets on the honeycomb lattice, *Phys. Rev. B* **104**, 064435 (2021).
- [50] B. Li, J.-Q. Yan, D. M. Pajerowski, E. Gordon, A.-M. Nedić, Y. Sizyuk, L. Ke, P. P. Orth, D. Vaknin, and R. J. McQueeney, Competing magnetic interactions in the antiferromagnetic topological insulator  $\text{MnBi}_2\text{Te}_4$ , *Phys. Rev. Lett.* **124**, 167204 (2020).
- [51] E. Gordon, V. Mkhitarian, H. Zhao, Y. Lee, and L. Ke, Magnetic interactions and spin excitations in van der Waals ferromagnet  $\text{VI}_3$ , *Journal of Physics D: Applied Physics* (2021).
- [52] H. Bethe, Termaufspaltung in kristallen, *Annalen der Physik* **395**, 133 (1929).
- [53] C. J. Ballhausen, *Introduction to ligand field theory* (McGraw-Hill, New York, 1962).
- [54] D. J. Newman and B. Ng, The superposition model of crystal fields, *Reports on Progress in Physics* **52**, 699 (1989).
- [55] M. Hutchings, Point-charge calculations of energy levels of magnetic ions in crystalline electric fields (Academic Press, 1964) pp. 227-273.
- [56] R. Skomski and J. M. D. Coey, *Permanent magnetism* (Institute of Physics Publishing, Bristol, 1999).
- [57] K. N. R. Taylor and M. I. Darby, *Physics of rare earth solids* (Chapman and Hall, London, 1972).
- [58] S. X. M. Riberolles, T. J. Slade, D. L. Abernathy, G. E. Granroth, B. Li, Y. Lee, P. C. Canfield, B. G. Ueland, L. Ke, and R. J. McQueeney, Competing magnetic energy scales in the topological flat-band ferrimagnet  $\text{tbmn}_6\text{sn}_6$  (2021), arXiv:2110.14713 [cond-mat.str-el].
- [59] Y. Lee, T. Kotani, and L. Ke, Role of nonlocality in exchange correlation for magnetic two-dimensional van der Waals materials, *Phys. Rev. B* **101**, 241409 (2020).
- [60] L. Ke and M. I. Katsnelson, Electron correlation effects on exchange interactions and spin excitations in 2D van der Waals materials, *npj Computational Materials* **7**, 1 (2021).
- [61] A. L. Kutepov, Electronic structure of van der waals ferromagnet  $\text{cri}_3$  from self-consistent vertex corrected *gw* approaches, *Phys. Rev. Materials* **5**, 083805 (2021).
- [62] F. D. M. Haldane, Model for a quantum hall effect without landau levels: Condensed-matter realization of the "parity anomaly", *Phys. Rev. Lett.* **61**, 2015 (1988).
- [63] G. hua Guo and H. bei Zhang, Magnetocrystalline anisotropy and spin reorientation transition of  $\text{HoMn}_6\text{Sn}_6$  compound, *Journal of Alloys and Compounds* **429**, 46 (2007).



## Supplementary information for:

### *Ab initio* studies of electronic structures and magnetic properties in $RMn_6Sn_6$ ( $R = \text{Gd, Tb, Dy, Ho, and Er}$ )

#### A. Comparison of band structures in $RMn_6Sn_6$ with $R = \text{Gd, Tb, Dy, Ho, and Er}$

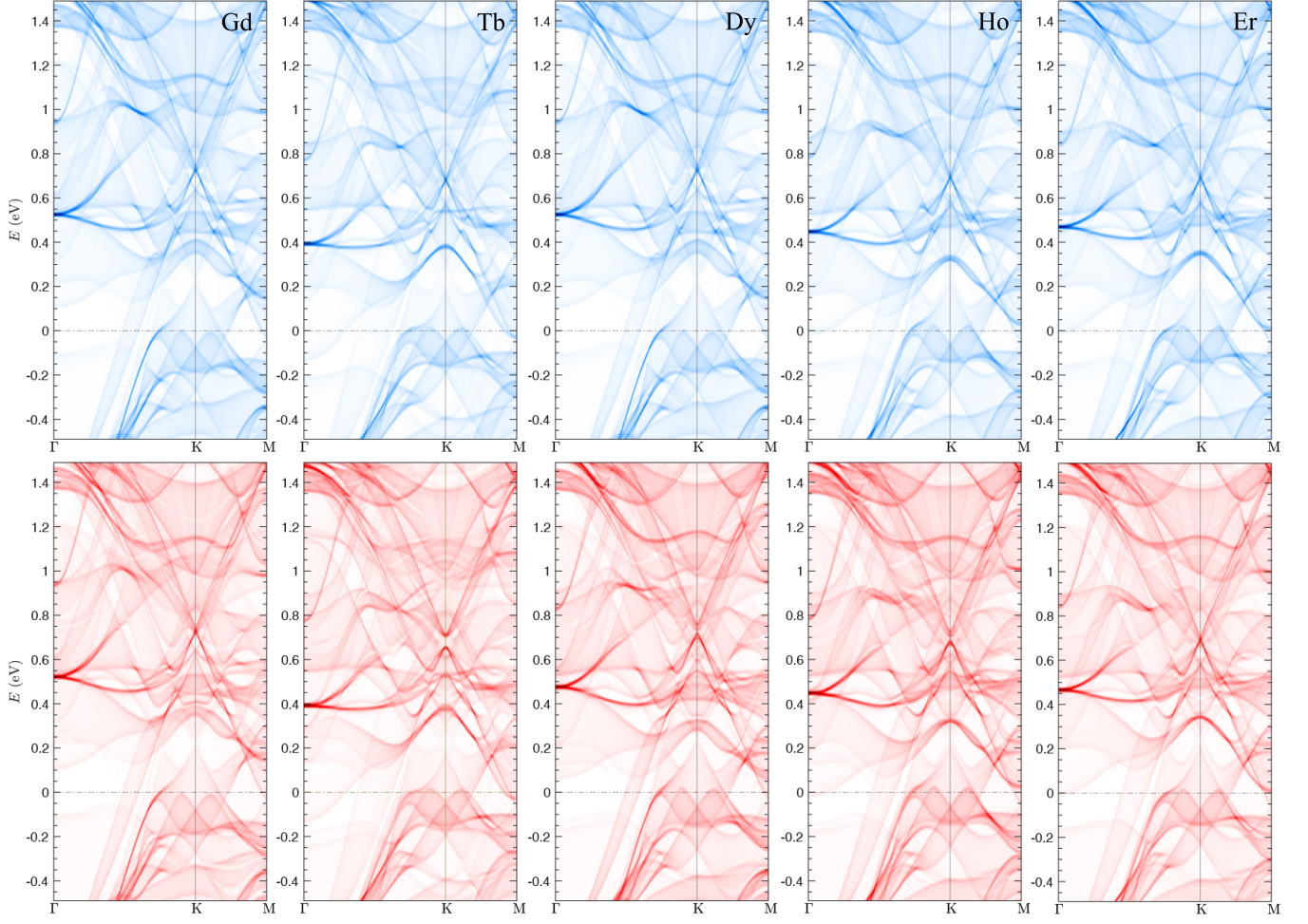


FIG. S1. The band structures projected on surface BZ near the Fermi level in  $RMn_6Sn_6$  with  $R = \text{Gd, Tb, Dy, Ho, and Er}$ , calculated without (in blue) and with (in red) SOC.  $R$ - $4f$  electrons are treated in the open-core approach in DFT and  $R$ - $4f$  electrons are configured to satisfy Hund's first rule. A Gaussian smearing of 5 meV is used for the  $k$ -dependent density of states. For the SOC cases, the spin quantization axis directions are set to be (or nearly) along the easy direction of each compound. More specifically,  $\theta_{\text{Gd}} = 90^\circ$ ,  $\theta_{\text{Tb}} = 0^\circ$ ,  $\theta_{\text{Dy}} = 45^\circ$ ,  $\theta_{\text{Ho}} = 49^\circ$ , and  $\theta_{\text{Er}} = 90^\circ$ . Overall, the band structures near  $E_F$ , consisting of non- $4f$  states, share great similarities in all compounds. Multiple DCs occur at  $K$ , below and above  $E_F$ . All of them show an intensive DC at  $\sim 0.7$  eV, which can be gapped by SOC, as we discussed above for  $R = \text{Tb and Ho}$ . The difference between these band structures can be attributed to the variations of lattice parameters and the strength of  $R$ - $5d$  moment and exchange splittings enhanced by various sizes of  $R$ - $4f$  spin.

TABLE S1. HoMn<sub>6</sub>Sn<sub>6</sub> band characters of six Dirac crossings near  $E_F$  at BZ corners  $K$ , as indicated in Fig. 6(a), resolved into atoms and Mn-3d orbitals. The majority and minority spin channels are referred to Mn sites.

Index	Minority Spin				Majority Spin	
	1	2	3	4	5	6
$E - E_F$ (eV)	-0.065	0.243	0.260	0.705	0.585	0.812
Ho	0.012	0.034	0.059	0.003	0.053	0.102
Mn	0.831	0.697	0.690	0.856	0.554	0.477
Sn	0.026	0.080	0.040	0.021	0.190	0.138
Interstitial	0.131	0.189	0.211	0.121	0.203	0.283
$d_{xy}$	0.009	0.026	0.001	0.091	0.075	0.000
$d_{yz}$	0.000	0.010	0.016	0.000	0.000	0.052
$d_{z^2}$	0.110	0.001	0.003	0.021	0.000	0.000
$d_{xz}$	0.002	0.000	0.093	0.000	0.000	0.011
$d_{x^2-y^2}$	0.015	0.076	0.000	0.025	0.012	0.000

TABLE S2. TbMn<sub>6</sub>Sn<sub>6</sub> band characters of six Dirac crossings near  $E_F$  at BZ corners  $K$ , as indicated in Fig. S2, resolved into atoms and Mn-3d orbitals. Majority and minority spin channels are referred to Mn sites.

Index	Minority Spin				Majority Spin	
	1	2	3	4	5	6
$E - E_F$ (eV)	-0.052	0.195	0.293	0.684	0.580	0.826
Tb	0.018	0.038	0.054	0.002	0.057	0.062
Mn	0.817	0.690	0.699	0.854	0.546	0.492
Sn	0.025	0.080	0.038	0.022	0.189	0.144
Interstitial	0.139	0.191	0.209	0.122	0.210	0.301
$d_{xy}$	0.009	0.025	0.001	0.092	0.073	0.000
$d_{yz}$	0.002	0.011	0.015	0.000	0.000	0.054
$d_{z^2}$	0.105	0.001	0.007	0.021	0.000	0.002
$d_{xz}$	0.004	0.002	0.090	0.000	0.000	0.011
$d_{x^2-y^2}$	0.015	0.076	0.002	0.024	0.012	0.000

### B. Orbital characters of Dirac crossings near $E_F$

To understand the  $k_z$  dependence of surface bands and how the Dirac crossings and SOC-induced gaps evolve with spin orientation, we analyze the corresponding orbital characters at these band crossings. Figure 6(a) shows the band structure in HoMn<sub>6</sub>Sn<sub>6</sub> calculated without SOC along the high symmetry path  $\Gamma$ - $K$ - $M$  ( $k_z = 0$ ). Six DCs, indexed as 1–6 in Fig. 6(a), occurs within the energy window; four (DC1–DC4) in minority Mn-spin channel, and two (DC5, DC6) in the majority Mn-spin channel. The band characters of these DCs are resolved into atoms and Mn- $d$  orbitals, as listed in Table S1.

Band characters are dominated by Mn- $d$  orbitals while showing hybridization with Ho and Sn sites. In comparison to other crossings, two DCs in the majority spin channel, DC5 and DC6, have more substantial amounts of contributions from Ho and Sn, especially the latter, resulting in a stronger  $k_z$  dependence, as shown in Fig. 5. In contrast, DC4 and DC1 in the minority spin channel, consisting of the least amount of Sn and Ho characters, show strong intensity in Fig. S1.

The size of the SOC-induced gap and its dependence on spin quantization direction can be understood by further resolving the band characters into Mn- $d$  orbitals. DC4 consists  $d_{xy}$  ( $|m = -2\rangle$ ),  $d_{z^2}$  ( $|m = 0\rangle$ ), and  $d_{x^2-y^2}$  ( $|m = 2\rangle$ ) characters. The SOC Hamiltonian, more specifically, the  $L_z$  operator, couples  $|m = \pm 2\rangle$  states and effectively opens up a gap. On the other hand, DC1 consists of more  $|m = 0\rangle$  states and less  $|m = \pm 2\rangle$  states, resulting in a much smaller SOC-induced gap. DC5 contains Mn- $|\pm 2\rangle$  states and also a substantial amount of Sn- $p$  states, which have a large SOC constant, giving a large gap, as shown in Fig. 6(b).

TbMn<sub>6</sub>Sn<sub>6</sub> shows the similar orbital characters, as shown in Table S1 and Fig. S2.



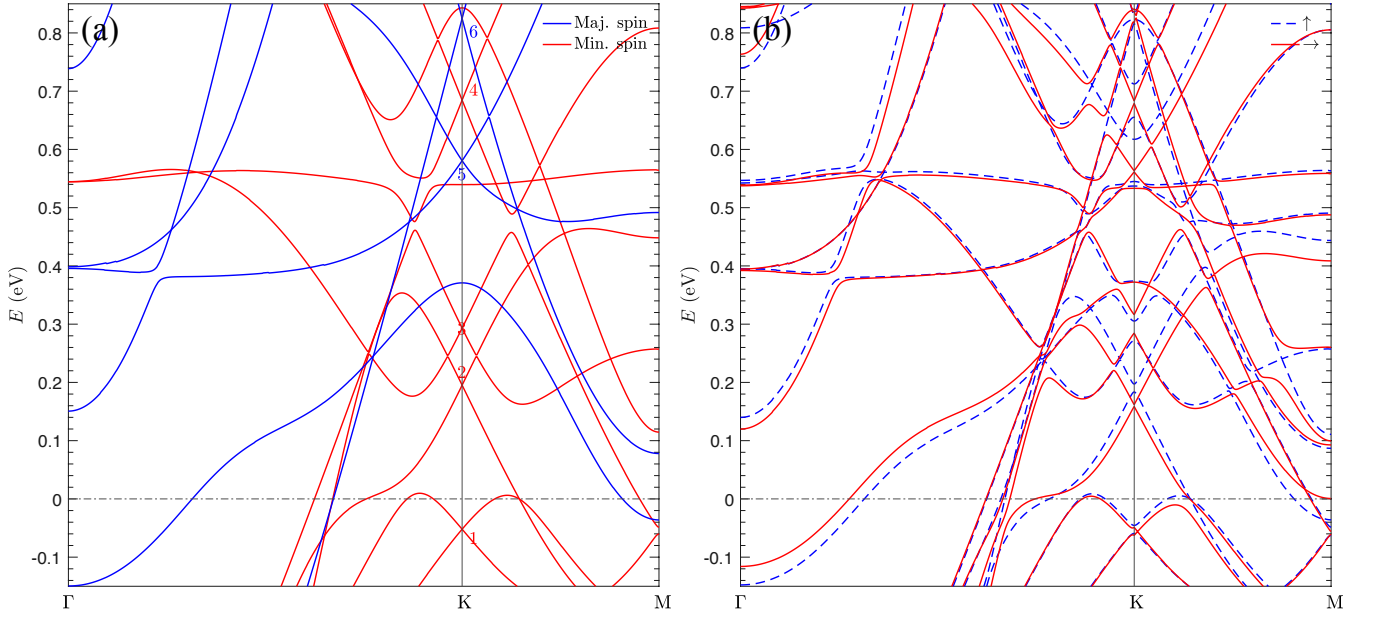


FIG. S2. Band structure near  $E_F$  in  $\text{TbMn}_6\text{Sn}_6$  calculated (a) without SOC and (b) with SOC. In panel (a), the majority-spin and minority-spin, referred to Mn site, are in blue and red, respectively. In panel (b), the band structures are calculated with the spin-quantization axis along the out-of-plane (blue dashed line) and in-plane (red solid line) directions. Both magnetic sublattices are ordered. The gap sizes depend on spin orientations.

### C. Origin of easy-plane Mn anisotropy: Combined effects of Mn-3d spin polarization and large Sn-4p SOC

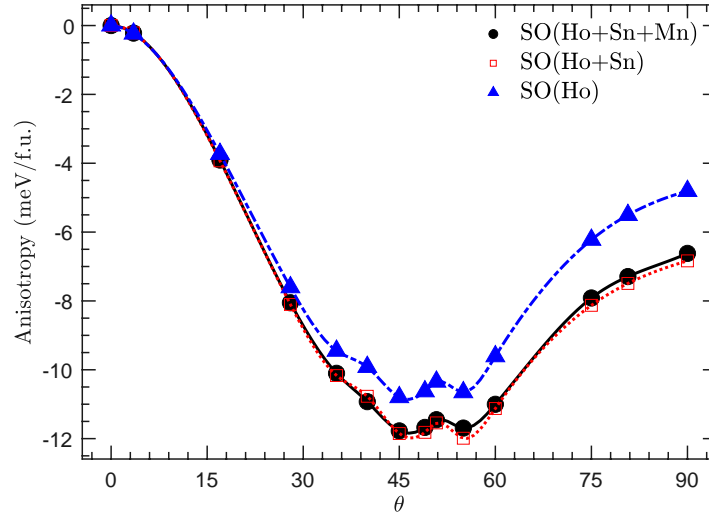


FIG. S3. Variation of magnetic energy (in meV/f.u.) as a function of spin-quantization-axis rotation in  $\text{HoMn}_6\text{Sn}_6$ , calculated with and without turning on SOC on Sn and Mn sites.  $\theta$  is the angle between the spin direction and the out-of-plane direction. The black circles denote the regular full-SOC calculations with SOC turning on all sublattices. The red squares are calculated with SOC on Ho and Sn sublattices only, barely deviating from the full-SOC calculations (black circles). The blue triangles denote the calculations with Ho SOC only, showing the Ho sublattice, by itself, prefers the  $\sim \theta = 49^\circ$  orientation. Turning off Sn SOC also increases  $E(\theta = 90^\circ)$  by  $\sim 2$  meV/f.u., which is the value of the above discussed easy-plane Mn anisotropy. Thus, Mn MA originates from the interplay between the Mn-3d spin polarization and the large Sn-4p SOC.

#### D. Dependence of Mn spin magnetic moments on Hubbard $U$ in DFT+ $U$ : The AMF and FLL double-counting schemes

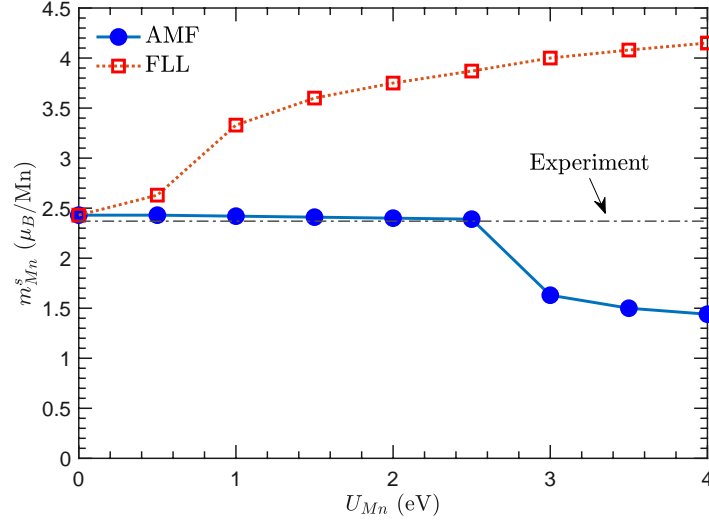


FIG. S4. The dependence of on-site Mn spin magnetic moment  $m_{Mn}^s$  in  $TbMn_6Sn_6$  on  $U_{Mn}$  calculated within DFT+ $U$  using the around-mean-field (AMF) and the fully-localized-limit (FLL) double-counting schemes. Hubbard  $U$  is applied on Mn-3d orbitals. The calculations are performed in a full-potential LMTO method without SOC, confirming the same trends we obtained in WIEN2K. The Mn spin moment  $m_{Mn}^s$  calculated in the AMF scheme agrees well with the experiment with  $U = 0$ –2.5 eV, while the FLL scheme tends to overestimate  $m_{Mn}^s$ .